Supplementary Information for "Detecting spin bath polarization with quantum quench phase shifts of single spins in diamond"

Paul C. Jerger,[1] Yu-Xin Wang (王语馨),[1] Mykyta Onizhuk,[1,2] Benjamin S. Soloway,[1] Michael T. Solomon,[1,3] Christopher Egerstrom,[1,3] F. Joseph Heremans,[1,3] Giulia Galli,[1,2,3] Aashish A. Clerk,[1,3] and David D. Awschalom[1,3,4]

[1] *Pritzker School of Molecular Engineering, University of Chicago, Chicago, Illinois 60637, USA*

[2] *Department of Chemistry, University of Chicago, Chicago, Illinois 60637, USA*

[3] *Center for Molecular Engineering and Materials Science Division, Argonne National Laboratory, Lemont, Illinois 60439, USA*

[4] *Department of Physics, University of Chicago, Chicago, Illinois 60637, USA*

(Dated: September 27, 2023)

CONTENTS

I. EXPERIMENTAL APPARATUS

All data presented was taken on single NV centers in an electronic grade, natural ^{13}C abundance, (100)-oriented diamond procured from Element Six. The residual nitrogen density is < 5 ppb. To create NV centers, the sample was first irradiated with 2 MeV electrons at a density of 3×10^{14} cm^{-2}, creating vacancies, followed by annealing for 2 hrs at 850 C in argon forming gas, which mobilizes vacancies and forms defect centers.

The confocal microscope setup used to image the NV centers is custom-built. A linearly polarized 532 nm laser (HÜBNER Photonics) is pulsed using a double-passed acousto-optic modulator (Gooch & Housego), exhibiting an extinction ratio > 60 dB. The laser is focused onto the diamond sample using an objective (Olympus MPLFLN100x) with NA 0.9 and $> 85\%$ transmission over the visible spectrum. The NV photoluminescence (PL) is separated from the laser by a 550 nm longpass dichroic mirror, filtered through an 830 nm shortpass, and measured using an avalanche photodiode (PerkinElmer SPCM-AQR-16). The laser is rastered using a fast steering mirror (Newport Corp.), and single NV centers are identified by isolated PL peaks with optically detected magnetic resonance (ODMR) contrast. Spin rotations and spin locking around the x- and y-axes of the Bloch sphere are performed using a vector signal generator (SRS SG396) at ~ 2.001 GHz. To implement both fast spin rotations (~ 8 MHz) and slow spin locking (~ 300 kHz) at the same frequency, this pathway is split, independently attenuated and switched, then recombined. A second signal generator (SRS SG384) provides microwaves to drive the $|0\rangle \leftrightarrow |+1\rangle$ transition at 3.739 GHz. After multiplexing, the microwaves are amplified (Mini Circuits ZHL-16W-43+) and delivered to the sample by a coil of wire suspended between the objective and the diamond surface. Two permanent magnets (K&J Magnetics) on custom goniometers are used to apply the well-aligned 310.8 G magnetic field to the NV axis (section SII D). The timing of all equipment is synchronized using an arbitrary waveform generator (Tektronix 5014C, 1 GSa/s).

II. NV CHARACTERIZATION MEASUREMENTS

A. NV repolarization

The NV center state must be initialized optically before each experiment. To estimate the intersystem crossing repolarization rate, we track PL during a green laser pulse. For $\sim 450\,\mu$W of laser power, the collected PL when initialized into bright ($|0\rangle$) and dark ($|-1\rangle$) states converges after $1\,\mu$s. These dynamics play a minor role in the bath evolution, since the NV spin is not instantaneously reinitialized to the decoupled $|0\rangle$ state after a spin-echo sequence. The correction is already too small to be observed in our experiments, but if desired, the repolarization rate could be increased by using higher laser powers.

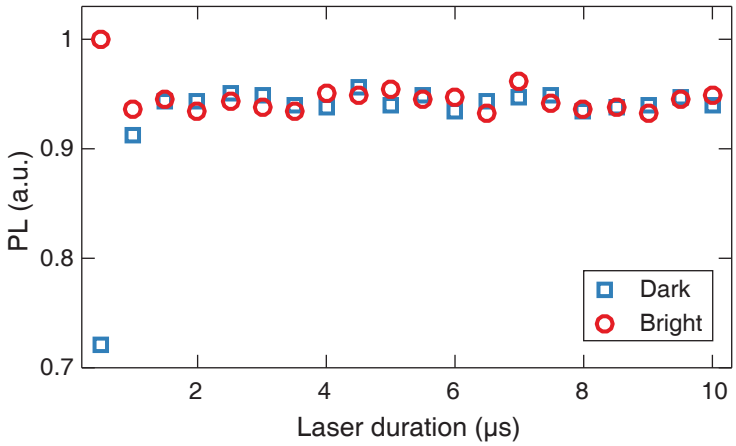

FIG. S1. PL as a function of time after green laser excitation. The pulse sequence consists of laser pulses with (dark) and without (bright) an intermediate microwave π pulse. The NV spin is observed to reinitialize within $11\,\mu$s.

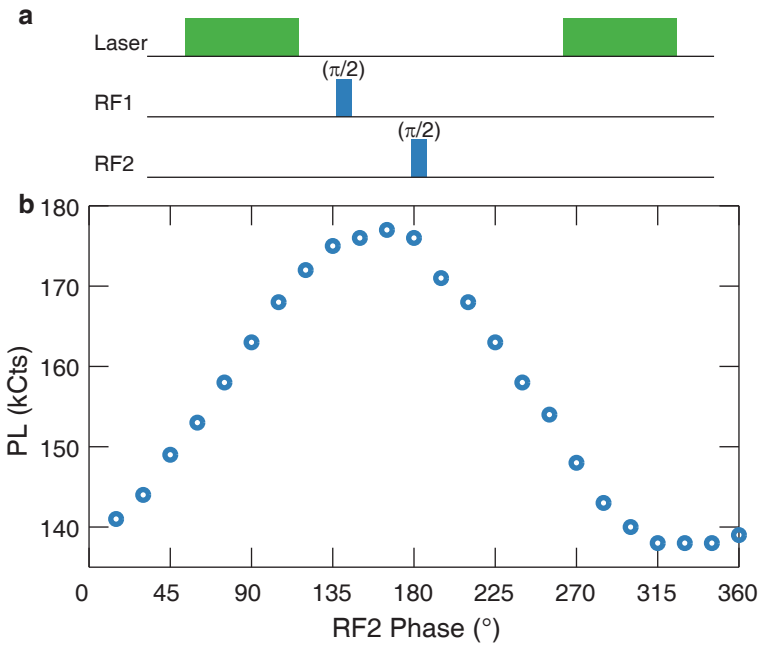

FIG. S2. (a) Pulse sequence and (b) data for calibrating the phase difference due to the two different rf paths. The minimum (maximum) of the counts indicate where the phase difference at the sample is 0 (180) degrees.

B. rf phase calibration

The phase of the spin-locking and spin rotations must be 90 degrees out of phase. While the microwaves used for spin-locking and spin rotations are generated with the same source, the microwaves go through different rf paths, leading to phase differences at the sample. To calibrate the phase difference, we use the sequence in Fig. S2a, consisting of a $\pi/2$ pulse from RF1 followed by a $\pi/2$ pulse from RF2. A cumulative π pulse converting the NV population from $m_s = 0$ to $m_s = -1$ occurs only when the phase difference is zero. Since the NV $m_s = 0$ is bright and $m_s = -1$ is dark after excitation, zero phase difference can be identified by a minimum of counts in Fig. S2b.

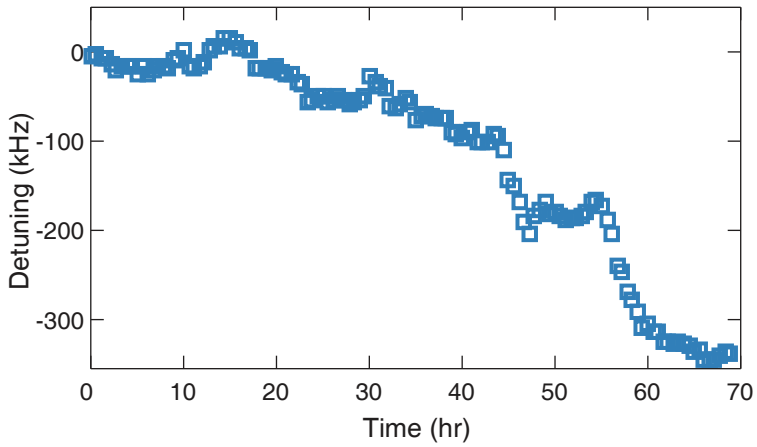

FIG. S3. Detuning of the NV resonance frequency as a function of time. The resonance frequency was measured by fitting the ODMR to a Gaussian.

C. NV resonance stabilization

We stabilize the NV spin transition frequencies to maintain both ESR and Hartmann-Hahn double resonance conditions. This is accomplished in two parts: thermal stabilization and resonance tracking. Thermal fluctuations at the sample and microscope objective are reduced by applying temperature feedback, which holds the apparatus slightly above room temperature. The measured drift is < 0.02 K over the course of most experiments. More consequentially, the permanent magnets are not temperature-controlled, and so fluctuations in room temperature still induce drift of the resonance as the Zeeman field fluctuates. We compensate for the magnetic field drift by periodically performing an ODMR scan over a single hyperfine branch of the NV transition. The narrow linewidth (~ 200 kHz) and low rf power enable us to measure the transition frequency to within 10 kHz in a 4 min measurement. ODMR tracking is repeated each 40-60 min to monitor drift. Fig. S3 shows a typical result from multiple days of resonance tracking, where the cumulative shift is greater than the spin linewidth, but the difference between sequential measurements is 10 kHz on average and never exceeds 35 kHz. To estimate the impact on the spin-locking frequency, we calculate the generalized spin-locking Rabi frequency,

$$\tilde{\Omega}_{SL} = \sqrt{\Omega_{SL}^2 + \delta^2}.$$

When the spin locking drive $\Omega_{SL} = 2\pi \times 335$ kHz, and assuming the maximal detuning of $\delta = 35$ kHz, the deviation $(\tilde{\Omega}_{SL} - \Omega_{SL})/\Omega_{SL}$ is $< 1\%$.

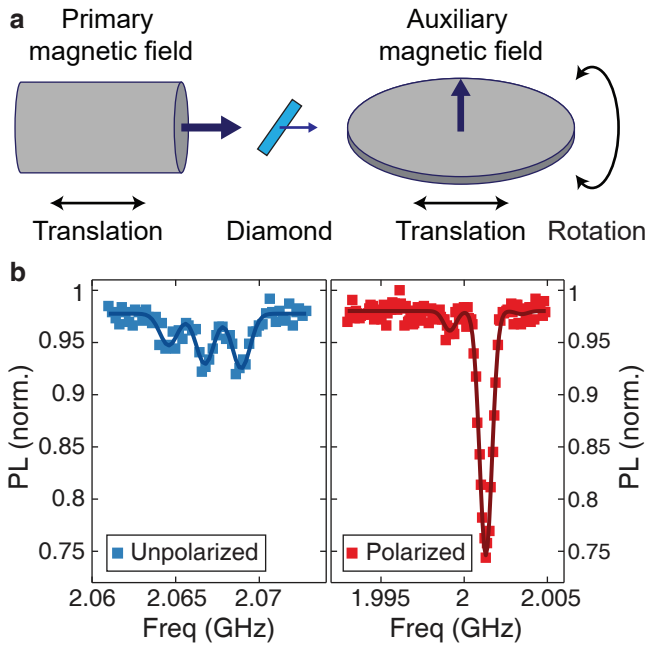

FIG. S4. Magnetic field alignment calibration. (a) The primary magnet establishes the field magnitude of 310 G and is aligned to the NV axis within 2°. The auxiliary magnet applies a field perpendicular to the NV axis, and is rotated and translated until the misalignment is minimized. (b) ODMR spectrum with magnetic field misaligned (left) and aligned (right) to the NV quantization axis. When aligned, the ^{14}N is optically polarized into the $m_I = +1$ state.

D. Magnetic field alignment

The external magnetic field is created by a system of two permanent magnets, whose arrangement is illustrated in the schematic of Fig. S4a. The alignment procedure is as follows. First, the strong, main, cylindrical magnet is mounted on a translation stage that is oriented close to the target NV axis ($\vec{n}_{NV}$), which lies at a 54.7° angle to the (100) surface of the diamond sample. The magnet position is tuned to reach a 310 G field magnitude, and is determined to be approximately 2° misaligned to $\vec{n}_{NV}$ by measuring both ground state transition frequencies [1]. This implies a residual off-axis field of ≈ 10 G. To cancel this remaining component, we introduce an auxiliary magnet. This magnet is a wide disc with axis $\vec{n}_{aux}$ oriented out of its plane. Thus, when it is positioned with its center on $\vec{n}_{NV}$ and $\vec{n}_{aux} \perp \vec{n}_{NV}$, B_{aux} at the location of the NV also points perpendicular to $\vec{n}_{NV}$. A 3D-printed brace holds it to a rotation mount, which allows it to be rotated around $\vec{n}_{NV}$ without moving its center. The auxiliary magnet is first rotated to find the angle at which it best cancels the residual perpendicular magnetic field for the NV center, and then translated until the best amplitude is found. As the alignment improves, the NV ODMR transitions display increasing nitrogen nuclear polarization (Fig. S4b) going from very little polarization with just the main magnet (left) to polarization 90-94% with a calibrated auxiliary magnet (right). Once the alignment is better than 1° misaligned, the polarization ratio of the center and right dips is used as feedback to optimize the auxiliary magnet position.

E. Candidate NV screening

Approximately 50 NV centers were identified and evaluated for suitable local nuclear spin baths, of which NVs A and B were chosen. As described in the main text, the initial, more rapid screening metric was the ODMR spectrum at low rf power. This reveals NV centers with strongly coupled nuclei and provides insight into the T_2^* coherence time, which is $\propto \Gamma^{-1}$ for linewidth Γ. After confirming that an NV had a $\Gamma/2\pi < 500$ kHz, we performed a secondary test by measuring $\langle X \rangle$ after a spin echo, spanning 3-4 nuclear Larmor periods. NVs with Gaussian baths are expected to show periodic decay and recovery patterns, which makes the observation of nearly periodic coherence dips a necessary but not sufficient condition for a Gaussian bath. Thus, we ruled out NVs with obvious aperiodic behavior in this measurement, regardless of ODMR linewidth. The remaining NVs were investigated using XY8 techniques (as detailed in the main text) to most thoroughly assess their spin baths.

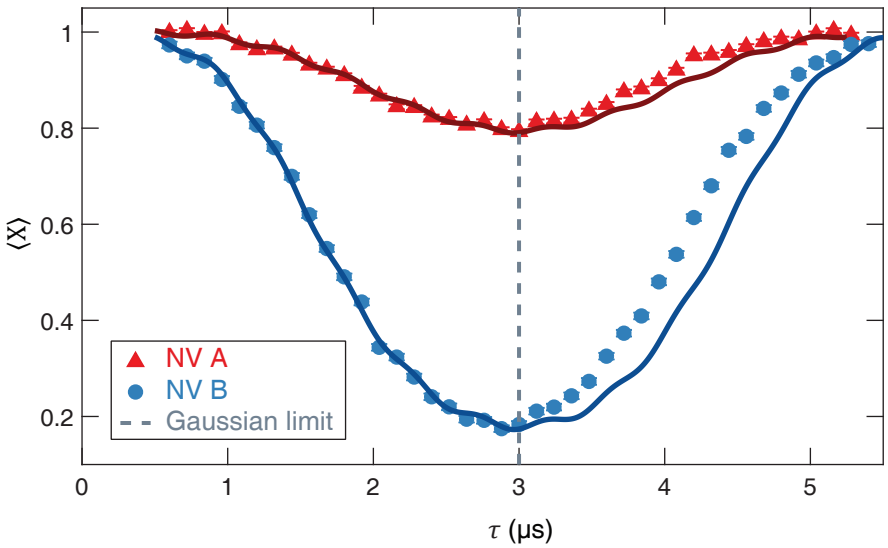

FIG. S5. Measurement of ϵ for both NVs used in the main text. The fits are performed on data for $\tau \leq 3$ μs, after which the Gaussian approximation begins to break down. The small oscillating component is attributed to residual off-resonant NV population.

F. Characterizing ϵ

In order to more precisely measure ϵ for NVs A and B used in the main text, we measured $\langle X \rangle$ with finer time resolution and shorter microwave pulses. The data is fit to

$$\langle X(\tau) \rangle = e^{-\chi(\tau)},$$
$$\chi(\tau) = 2\epsilon \sin^4\left(\frac{\omega_L \tau}{4}\right),$$

where the equation for χ is Eq. (7) in the main text. ω_L is determined in ODMR measurements, and a normalization factor is additionally fit for NV B to account for pulse imperfections. A small cosine term at 2.2 MHz is added in each case, which originates from residual off-resonant NV population. The fit values are $\epsilon_A = 0.115(3)$ and $\epsilon_B = 0.852(16)$. We fit only to the data in the regime where non-Gaussian deviations are negligible ($\tau \lesssim 3$ μs; Fig. 3e), as non-Gaussian contributions modify the amplitude and frequency of the oscillations at longer times.

We can compare the measured ϵ values to those calculated using the individual hyperfine couplings extracted from XY8. The calculated values are $\tilde{\epsilon}_A = 0.094(3)$ and $\tilde{\epsilon}_B = 0.77(1)$, but underestimate the true values, as they do not include many nearby but unresolved nuclear spins. To estimate the expected contribution from the remaining spins, we simulate 10^3 random clusters of ^{13}C and remove all the spins with $A_\perp$ large enough to be detected in XY8. As a rough estimate of the detection limit, we use half of the smallest $A_\perp$ measured by the corresponding XY8 sequence (i.e., 22 kHz for XY8-1 on NV B, and 10 kHz for XY8-2 on NV A). Based on these limits, we compute additional contributions to ϵ of $\epsilon'_A = 0.014(2)$ and $\epsilon'_B = 0.033(7)$, with the uncertainties representing the standard deviation over 10^3 simulated spin clusters. The observed $\epsilon_A = 0.115(3)$ compares well with $\tilde{\epsilon}_A + \epsilon'_A = 0.108(4)$; likewise, $\epsilon_B = 0.852(16)$ compares well with $\tilde{\epsilon}_B + \epsilon'_B = 0.80(2)$.

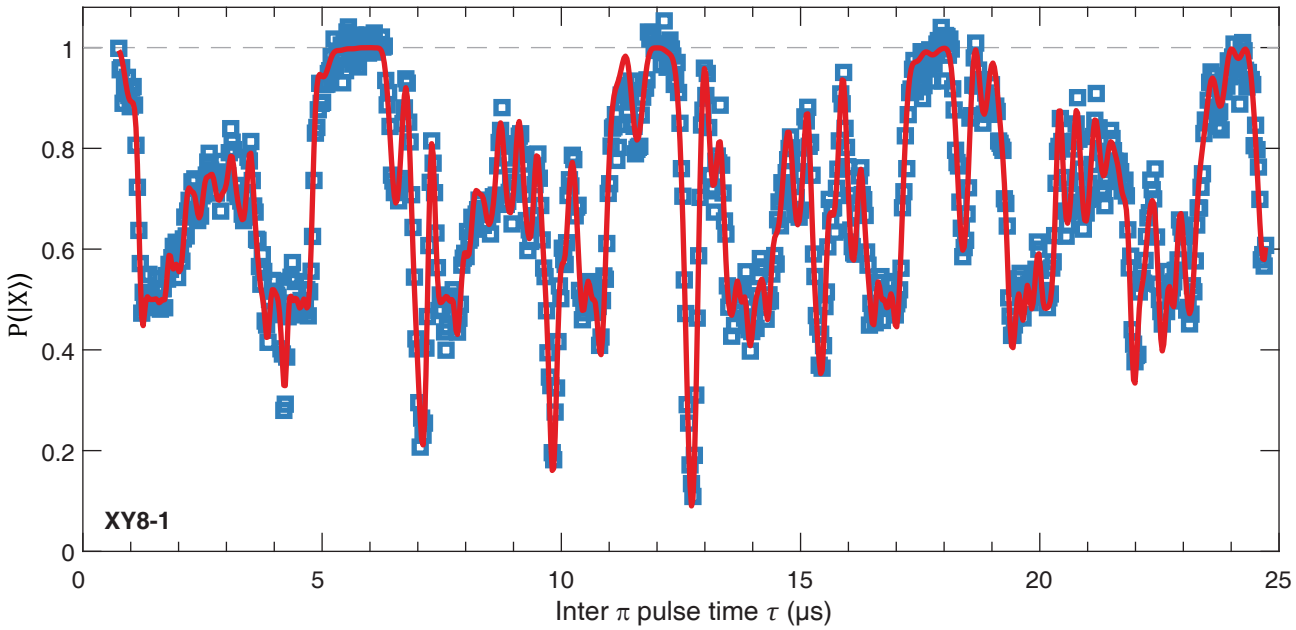

FIG. S6. Additional XY8-1 data and fit for NV B. Best-fit parameters are included in Table I.

III. XY8 DATA

A. XY8 fitting procedure

The nuclear hyperfine parameters were extracted as follows. First, using the PyCCE [2] package, we generated 10^4 random nuclear spin configurations and computed their expected XY8 signal. For both of the NVs used in the main text, we found a closest matching random nuclear spin configuration and used it as an initial guess for the fitting procedure. We then fit the experimental coherence to the analytical expression [3]:

$$\langle X\rangle = \prod_i 1 - \left(1 - \hat{n}_0^{(i)}\hat{n}_{-1}^{(i)}\right)\sin^2\frac{N\phi_i}{2}, \tag{S1}$$

where

$$\cos\phi_i = \cos\alpha_i\cos\beta_i - m_z^{(i)}\sin\alpha_i\sin\beta_i, \tag{S2}$$

$$1 - \hat{n}_0^{(i)}\hat{n}_{-1}^{(i)} = \left(m_x^{(i)}\right)^2\frac{(1-\cos\alpha_i)(1-\cos\beta_i)}{1+\cos\phi_i}. \tag{S3}$$

Here, $m_x^{(i)} = \frac{a_\perp^{(i)}}{\tilde{w}^{(i)}}$ and $m_z^{(i)} = \frac{a_\parallel^{(i)}+w_L}{\tilde{w}^{(i)}}$ using $\tilde{w}^{(i)} = \sqrt{(a_\parallel^{(i)}+w_L)^2 + (a_\perp^{(i)})^2}$; angles are $\alpha_i = \tilde{w}^{(i)}\tau$, $\beta_i = w_L\tau$ for each ith nuclear spin. Starting from one nuclear spin, we increase number of spins by one in the fitting procedure until the fit deviation from the experimental data stops decreasing. We then check the robustness of the fit by removing each of the identified nuclear spins in turn, and for all remaining nuclear spins we check whether the identified parameters have shifted. Only the nuclear spins which are validated with the leave-one-out procedure are reported.

B. XY8 data for NV B

XY8-1 data for NV B, along with the best-fit coherence envelope, is shown in Fig. S6. XY8-1 is suitable for this NV, instead of XY8-2 as used for NV A, since the couplings of nearby spins are larger than NV A's.

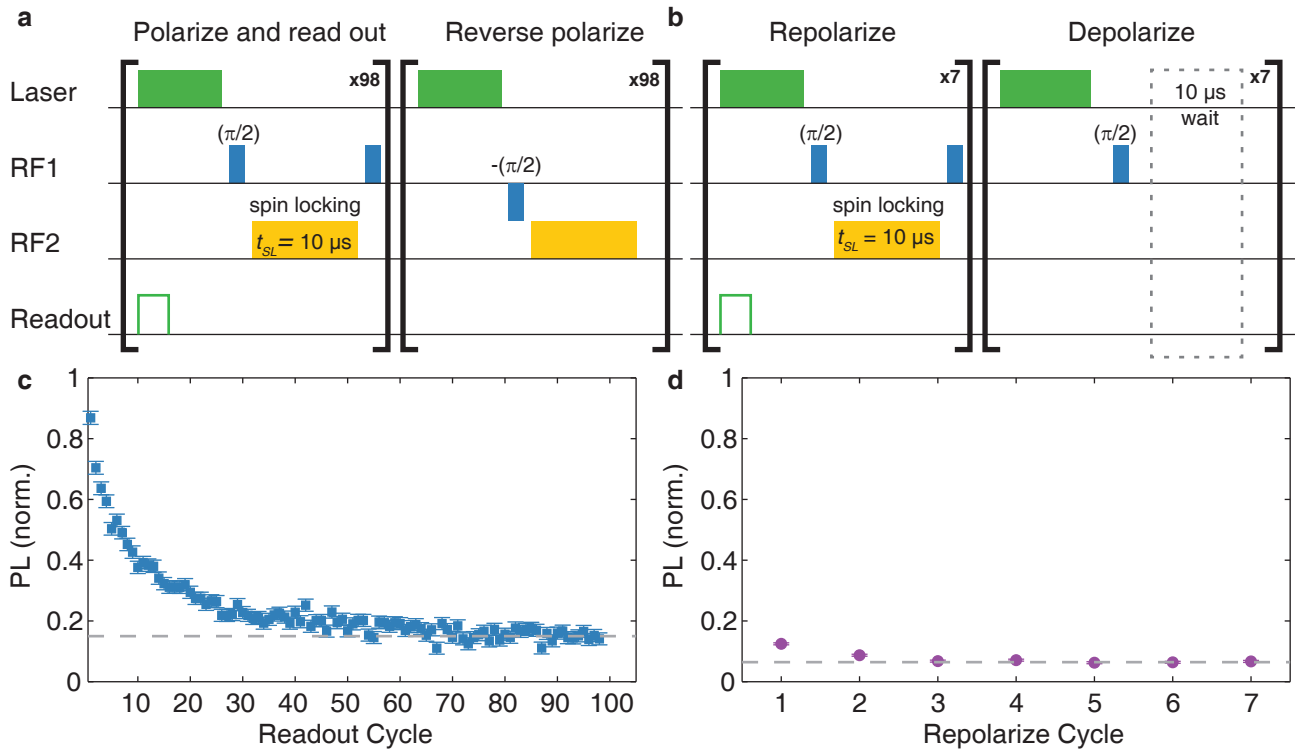

FIG. S7. PROPI measurements to characterize bath polarization dynamics, using NV A. (a) shows the canonical PROPI pulse sequence: the bath is polarized in one direction (in this case, via NOVEL) and then polarized in the opposite direction, while checking the magnitude of the NV polarization via PL at each NOVEL repetition. If the NV exchanges polarization with the bath, PL is initially high and then declines as the bath saturates under repeated polarization cycles. This behavior is observed in (c), confirming efficient polarization of the nearby bath spins. Roughly 75 cycles of NOVEL are needed to fully reverse polarize the bath once initially polarized. (b) shows the modified PROPI sequence used to identify the number of cycles N sufficient to restore maximum polarization after delays and spin operations. In place of reverse polarizing, a mix of laser pulses, rf pulses, and long wait periods are alternated to approximate the effect of PSE measurements. PL is then measured during the NOVEL cycles that repolarize the bath. (d) shows that the bath returns to equilibrium after $N = 3$ repetitions, but we use $N = 5$ to be conservative.

IV. NUCLEAR POLARIZATION CHARACTERIZATION

We use the Polarization ReadOut by Polarization Inversion (PROPI) sequence [4] to independently verify that our NOVEL sequence is correctly transferring polarization to the bath. In PROPI, the nuclear spin bath polarization surrounding an NV center is read out by inducing polarization in the opposite direction using the NV, and monitoring the decay of PL as the bath saturates to its new equilibrium. Fig. S7a shows the pulse sequence of the basic PROPI sequence. First, the bath is polarized along an axis using any method; in this case, 98 repetitions of our NOVEL sequence. To detect polarization, the bath is then polarized in the reverse direction with an efficient method; we demonstrate using the NOVEL sequence again. Before reinitializing the NV center for each repolarization cycle, the spin is rotated to the z axis, so that the PL is minimized if it remains in its original state. Thus, if polarization is transferred to the bath, PL will be high. Since the polarization transfer occurs more quickly than bath spin depolarization or diffusion, the polarization saturates, evidenced by a decay of the PL with repeated NOVEL cycles (Fig. S7c). This characteristic decay indicates that the NV environment is indeed being polarized and reaching equilibrium.

We then use PROPI to inform our choice of the number of NOVEL repetitions, N. Specifically, we use it to gauge the depolarizing effect of laser illumination, spin rotations, and extended delays in the pulse sequence. In Fig. S7b, we diagram a sequence which replaces the NOVEL reverse polarization with alternating laser pulses, $\pi/2$ rotations, and 10-μs wait periods (the "depolarize" cycles). The depolarization from this sequence should be comparable to that of a PSE measurement. In Fig. S7d, we observe that equilibrium is restored after three repolarization cycles. In the majority of our measurements, we use $N = 5$ to be conservative and ensure a stable equilibrium state.

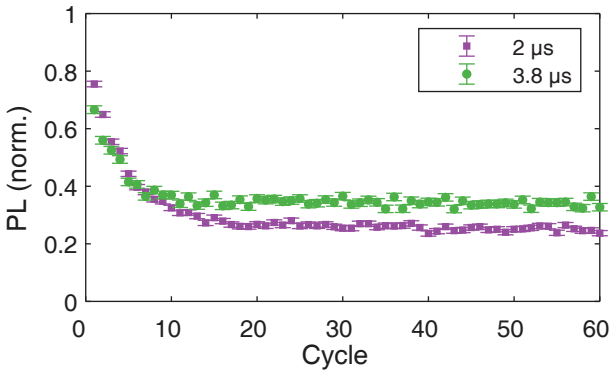

FIG. S8. PROPI measurements on NV A demonstrating sensitivity to NOVEL parameters. The two sequences are identical in construction except for the duration of the laser pulse, but show distinct PROPI decays. The PROPI signal is the integral of the decay portion above the long-time baseline, and so the two curves yield far different quantities. Note that the difference likely does not result from the additional laser exposure in itself, but rather the approximately half-Larmor-period additional evolution between each spin-locking pulse when the pulse length is 3.8 μs. Thus, a difference could reasonably appear when transverse polarization is significant, as we ultimately determine to be the case under these experimental conditions.

The observations in Fig. S7 hint at potential complexities in interpreting PROPI data. The quantitative polarization signal is computed to be the summed difference of the PL curve and the asymptotic level (dashed line in Fig. S7c). These readings can take upwards of 1 ms to acquire, which is long enough to permit some dynamics within the bath during the measurement. In addition, the apparent asymptotic level after 100 cycles in Fig. S7c (≈ 0.15) is significantly higher than the asymptote in Fig. S7d (≈ 0.05), where the bath is only ever polarized in one direction. This comparison suggests that PL in Fig. S7 would continue to decay for perhaps hundreds of cycles as the bath slowly equilibrates. Thus, there may be multiple timescales in the bath polarization dynamics, which raises the question of which asymptote is most appropriate to use for quantifying polarization.

We explore this direction further by slightly changing the PROPI parameters, shown in Fig. S8. The sequences follow Fig. S7a, except for using different laser pulse durations. Surprisingly, the two PROPI signals are clearly distinct, with the 2-μs pulse set starting with higher PL and reaching a lower asymptote than the 3.8-μs set. This seems to suggest that laser illumination is affecting the bath polarization, but more likely this effect is due to the additional 1.8 μs between spin-locking pulses, which is roughly half of the Larmor period. The extra bath evolution time should only matter if significant transverse polarization exists, and the findings in the main text reveal that transverse polarization can be quite large under these experimental conditions. Thus, the combination of these measurements offers another explanation for the elevated asymptote of the 3.8-μs data set: a substantial fraction of the NV coherence in each NOVEL cycle may be consumed to re-establish the same transverse polarization each cycle, without contributing to the axial polarization. It can be difficult to discern these phenomena within a single PROPI measurement, although transverse polarization should be negligible in systems where the Larmor frequency is much larger than the hyperfine couplings. In contrast, QPS measurements can provide direct insight into some of these polarization dynamics. The QPS signal is measured with a single spin echo on the timescale of a nuclear Larmor period, fast enough to ignore bath dynamics (apart from Larmor precession) during the measurement. Resolving both axial and transverse polarization components could clear up ambiguity about the source of the PROPI asymptotic signal and the state of the bath at intermediate times. Finally, its direct proportionality to the axial polarization is preferable to a relative measure summed over a series of measurements.

V. PHASE-RESOLVED SPIN ECHO SEQUENCE

A. Pulse sequences

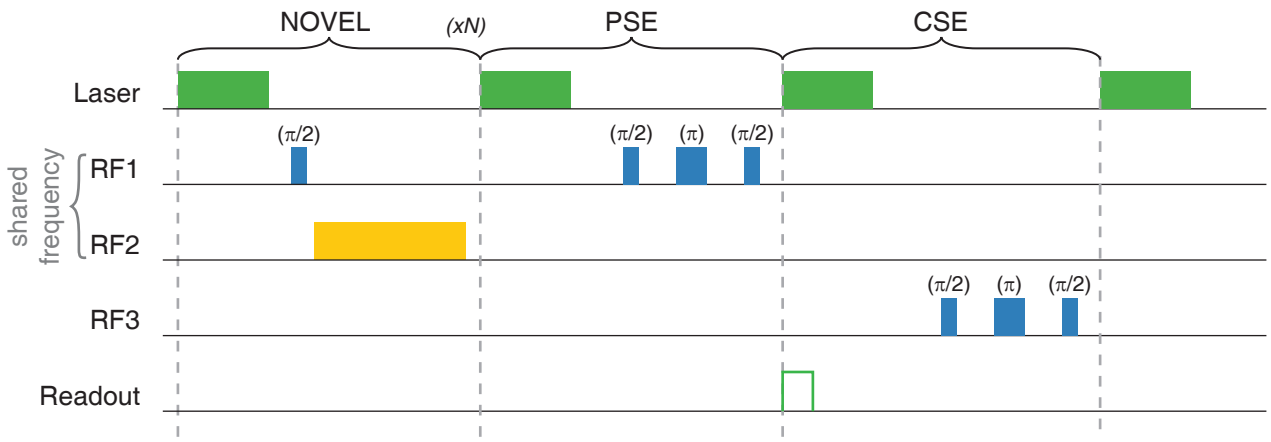

FIG. S9. Schematic of pulse sequence elements for a NOVEL+PSE+CSE measurement. RF1 and RF2 originate from the same signal generator and address the $|0\rangle \leftrightarrow |-1\rangle$ transition with different Rabi frequencies. RF3 addresses the $|0\rangle \leftrightarrow |+1\rangle$ transition. Readout of the NV electron spin is performed during the first 600 ns of the corresponding laser pulse.

Here we provide comprehensive detail on the phase-resolved spin echo (PSE) pulse sequence construction. The synchronized elements are diagrammed in Fig. S9, and the precise durations for a representative NOVEL+PSE+CSE measurement are listed in Table SI.

The NOVEL segment is repeated N times, and the entire sequence repeats upon completion for $10^6 - 10^7$ repetitions. Signal photons are collected during the first 600 ns of the designated readout laser pulse at the end of the PSE. The RF1 and RF3 pulse times differ due to increased rf attenuation at the higher frequency of RF3. τ is the same for PSE and CSE segments, measured between the centers of the corresponding initial and final $\pi/2$ pulses. Note that, to leading order, the phase of the NV state does not affect the bath evolution, and so the π pulse in the CSE should not be required; however, we maintain it to maximize the symmetry between the two spin echoes. t_{wait} consists of the delay between the final spin-locking pulse and the center of the initial PSE $\pi/2$ pulse. The initial $\pi/2$ pulses of the PSE and CSE must be separated by a multiple n of the Larmor period, which is accomplished by adjusting the delay to start the CSE segment. The smallest n which allows sufficient time for the PSE and ensuing spin initialization is used. Finally, t_{CSE} spans the interval from the center of the initial $\pi/2$ pulse of the CSE segment to the start of the first spin-locking pulse in the ensuing NOVEL. To ensure $t_{sum} = t_{wait} + nT_L + t_{CSE}$ is consistent as sequence parameters change, the final wait element of the CSE segment is adjusted as needed. For the sequence outlined in Table SI, the physically relevant parameters are $t_{SL} = 3{,}000$ ns, $\tau = 1{,}500$ ns, $t_{wait} = 5{,}500$ ns, and $t_{CSE} = 35{,}355$ ns. t_{CSE} is kept long so that t_{wait} can be increased without changing t_{sum}.

Segment	Element	Channel	Duration (ns)
NOVEL	Init. $\|0\rangle$	Laser	3800
	Settle	-	1000
	$\pi/2$	RF1	60
	Buffer	-	10
	Spin lock	RF2	3000
	Buffer	-	100
PSE	Init. $\|0\rangle$	Laser	3800
	Delay	-	1570
	$\pi/2$	RF1	60
	$\tau/2$	-	665
	π	RF1	110
	$\tau/2$	-	665
	$\pi/2$	RF1	60
	Buffer	-	100
	Readout & init. $\|0\rangle$	Laser	3800
CSE	Delay	-	505
	$\pi/2$	RF3	170
	$\tau/2$	-	515
	π	RF3	300
	$\tau/2$	-	515
	$\pi/2$	RF3	170
	Buffer	-	100
	Init. $\|0\rangle$	Laser	3800
	Wait	-	25000

TABLE SI. Timing parameters for an example NOVEL+PSE+CSE sequence. The NOVEL segment is repeated N times, and the entire sequence repeats upon completion for $10^6 - 10^7$ repetitions. Signal photons are collected during the first 600 ns of the designated readout laser pulse at the end of the PSE.

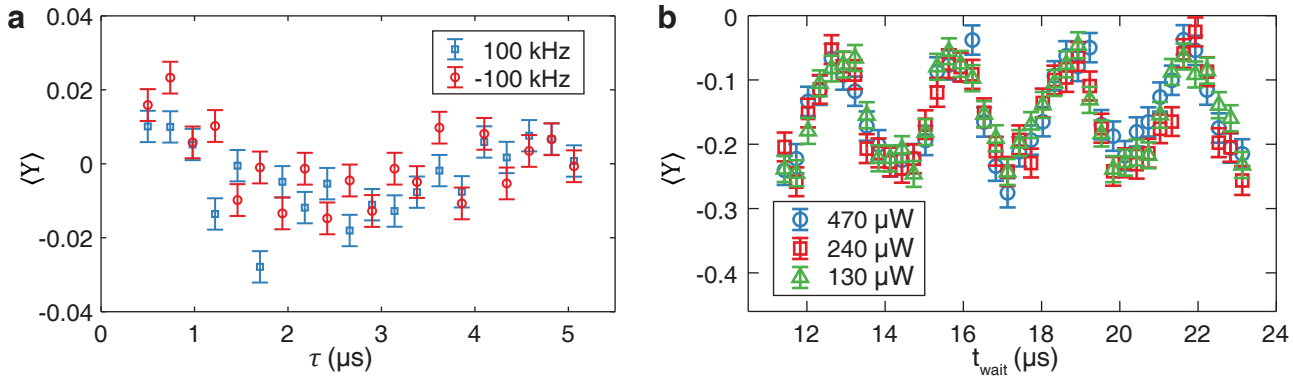

FIG. S10. (a) PSE measurement with deliberate detuning. The bath is left unpolarized. No significant signals are observed relative to the 0.1-0.2 scale of the QPS, and any coherent contributions are expected to change sign along with the detuning. The data were taken on NV A. (b) PSE measurements at different laser powers. To determine if the NV optical reset process plays a significant role in bath dephasing or depolarization, we perform a PSE measurement on NV B using 10-μs laser pulses at different optical powers ($t_{SL} = 3.5$ μs). No systematic difference is observed in the evolution.

B. Addressing sources of spurious signal

We evaluate potential sources of spurious phase accumulation to increase confidence in the QPS signals. First, we check the effect of a static detuning on RF1. We perform a PSE measurement without NOVEL, but with a deliberate $\pm$100 kHz detuning from resonance. While an ideal spin echo should cancel any static detuning, detuning also reduces the fidelity of resonant operations. As shown in Fig. S10(a), neither detuning induces significant deviation from zero. While a faint oscillation of amplitude < 0.01 may be present, it does not follow the sign of the detuning, as would be expected. This oscillation is not present for zero detuning, and the detuning in measurements is expected to be much less than 100 kHz, so any detuning contribution from drift or noise can be neglected.

A related effect is the influence of the nuclear polarization on the resonance. While the QPS originates from the $A_\perp$ components of the hyperfine interactions, the $A_\parallel$ components shift the resonance. To determine the magnitude of this shift, we alternate single NOVEL repetitions with a low rf power ODMR pulse. The resulting ODMR spectra are shown in Fig. S11. Both NV A and NV B show detectable resonance shifts, with deviations from the center frequency of ≈ 20 and ≈ 60 kHz, respectively. As we previously assessed the influence of larger detunings than measured here, the contributions from polarization-related resonance shifts can also be neglected.

We tested whether or not laser power had a significant effect on PSE signals. NV center illumination is known to play a role in nuclear spin polarization and coherence even for weakly coupled nuclear spins [5]. We performed PSE measurements using longer, 10-μs laser pulses and repeated them at three different powers. As shown in Fig. S10(b), no significant difference is observed, indicating that repolarization from NOVEL exceeds dephasing or depolarization from the green laser at the powers used here.

While not a spurious signal, the interpretation of the results in the main text is potentially complicated by the presence of the ^{14}N nucleus of the NV center, which is polarized as described in Sec. II D. However, unlike spin-$\frac{1}{2}$ ^{13}C nuclei, the ^{14}N nucleus has a large quadrupolar splitting of around 5 MHz. This quadrupolar splitting suppresses coherence envelope modulation [6], and along with it, the QPS. This assessment would not hold for NV centers containing ^{15}N nuclei, which are spin-$\frac{1}{2}$.

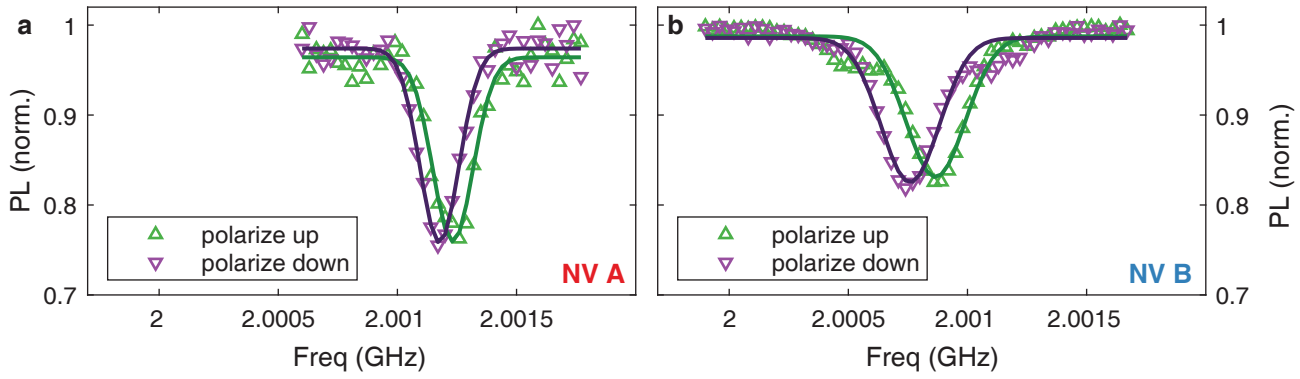

FIG. S11. ODMR spectra with polarized spin baths. Data is taken by alternating a single NOVEL segment with a low rf power ODMR measurement. The resonance shifts for ≈ 20 kHz on NV A (a) and ≈ 60 kHz for NV B (b).

C. Fit functions

In this section, we describe the fit procedure used to extract $\bar{p}_z$ and $\tilde{p}_\perp$ from sets of $\langle Y \rangle$, as in Fig. 4 of the main text. We restate several key equations from Sec. II of the main text:

$$\chi(\tau) = 2\epsilon \sin^4\left(\frac{\omega_L \tau}{4}\right),$$
$$\Phi_q(\tau) = \bar{p}_z \epsilon \sin^2\left(\frac{\omega_L \tau}{4}\right) \sin\left(\frac{\omega_L \tau}{2}\right),$$
$$\Phi_m(\tau) = \frac{2\sin^2\left(\frac{\omega_L \tau}{4}\right)}{\omega_L} \sum_k A_{\perp,j} \left(p_x^{(k)} \sin\left(\frac{\omega_L \tau}{2}\right) + p_y^{(k)} \cos\left(\frac{\omega_L \tau}{2}\right)\right).$$

Experimentally, we measure

$$\langle Y(\tau) \rangle = e^{-\chi(\tau)} \sin\left(\Phi_q(\tau) + \Phi_m(\tau)\right). \tag{S4}$$

When we choose $\tau = \pi/\omega_L$, this equation simplifies to

$$\langle Y \rangle = e^{-\epsilon/2} \sin\left(\frac{\bar{p}_z \epsilon}{2} + \frac{1}{\omega_L} \sum_j p_{x,j} A_{\perp,j}\right). \tag{S5}$$

By assuming $p_{x,j} = \tilde{p}_\perp \sin\left(\omega_L t_{wait} + \varphi\right)$, as described in the main text, we further reduce the expression for $\langle Y \rangle$ to

$$\langle Y(t_{wait}) \rangle = e^{-\epsilon/2} \sin\left(\frac{\bar{p}_z \epsilon}{2} + \frac{\tilde{p}_\perp}{\omega_L} \sin\left(\omega_L t_{wait} + \theta_0\right) \sum_j A_{\perp,j}\right). \tag{S6}$$

We fix ϵ as measured through $\langle X \rangle$ sweeps such as Fig. 2c, as well as $\sum_j A_{\perp,j}$ as calculated through Table I of the main text. $\omega_L = \gamma_n B_0$ is known, which makes Eq. S6 a three-parameter fit of $\bar{p}_z, \tilde{p}_\perp, \varphi$.

D. Measurement parameters

Fig.	NV	N	t_{SL} (μs)	τ (ns)	t_{wait} (ns)	t_{sum} (ns)
4a	A	5	2.75	1500	var.	59820
4a	A	5	3.75	1500	var.	54820
4b	B	5	2.75	1500	var.	59820
4b	B	5	4.5	1500	var.	51070
4e-f	A	5	2.75	var.	5600	59820
4e-f	B	5	2.75	var.	8000	59820
5	A	5	2.75	var.	5800	69560
6	B	5	4	var.	4880	var.

TABLE SII. Sequence parameters used to take data from the main text.

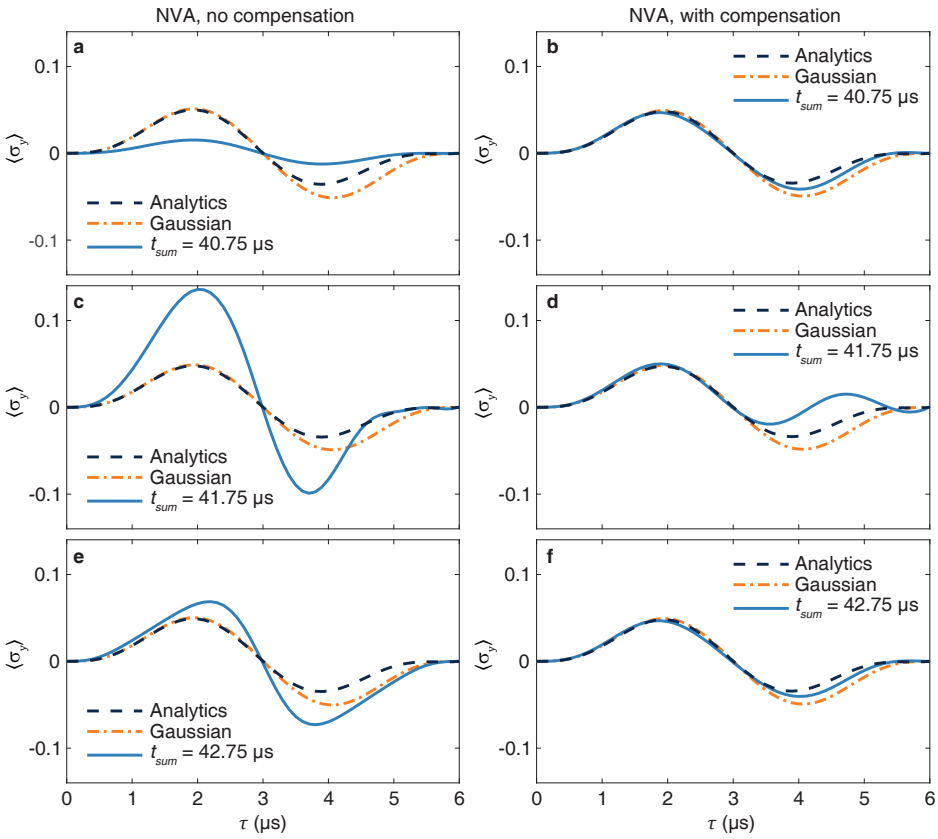

FIG. S12. Simulations comparing the analytics, Gaussian simulation, and numerics for the uncompensated (a,c,e) and compensated pulses (c,d,f) at three different values of t_{sum}

VI. COMPENSATING SPIN ECHO SEQUENCE

A. Simulations details

All simulations were carried out by numerically diagonalizing the time-independent model Hamiltonian and computing the corresponding propagators for each of the parts of the pulse sequence. Control pulses on the NV and NV reinitialization via laser pulse were assumed to be instantaneous, and rotating wave approximation was used for the NOVEL sequence. Interactions between nuclear spins were neglected.

To recover the steady-state polarization, each simulation included 50 cycles of the full experiment (5 NOVEL periods, PSE sequence, and CSE sequence when applicable). The nuclear and electron states, used in Figure 3, are recorded at the last cycle. The simulation included the following parameters: t_{wait} was varied between 5 and 20.6 μs, $t_{SL} = 3$ μs, $nT_L = 6$ μs.

Figures S12 and S13 show additional numerical data for the effect of compensating pulse at the phase signal of NV A. We observe a great match between numerical predictions using the whole sequence and analytical equations using the quench phase only when compensating pulse is applied. In the absence of compensating pulse, the behavior of the numerical curve deviates from the analytical expressions and thus cannot be used to recover the properties of the bath.

Figure S14 shows numerical simulations in comparison with the results from Fig. 4 of the main text. We observe an excellent agreement for NV A in both the observed signal ($\langle Y \rangle$) and derived quantities ($\tilde{p}_\perp$ and $\bar{p}_z$.). Still, we note that the observed parallel polarization consistently exceeds the numerical simulations by around 10%. This may reflect the contributions of the unresolved bath spins, which collectively account for 18% of ϵ_A and are not captured in the simulations.

NV B shows worse agreement with the theory in the $\langle Y \rangle$ simulations, hinting that not all relevant nuclear spins were determined with dynamical decoupling spectroscopy, or the internuclear interactions play non-negligible role.

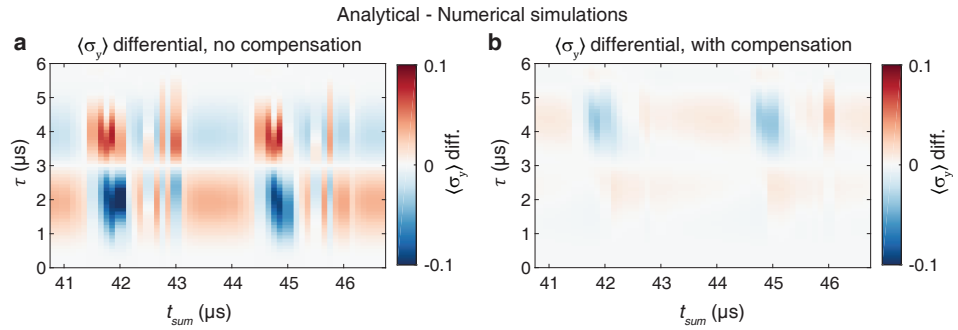

FIG. S13. Colormap showing the $\langle \hat{\sigma}_y \rangle$ differential between analytical and numerical simulations for the uncompensated (a) and compensated (b) sequence.

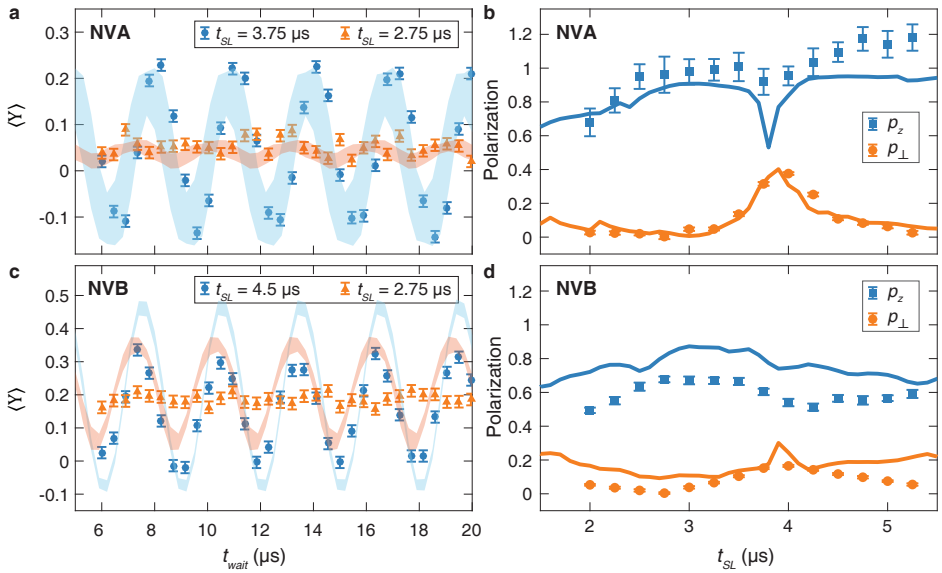

FIG. S14. Simulations for the Figure 4 in the main text. Phase evolution with τ =1.5 μs on NVs A (a) and B (c) as with respect to t_{wait}, and for several t_{SL}. Points represent experimental results, shaded areas - calculations for varied t_{sum}. Bath polarization for NVs A (b) and B (d). Solid lines represent numerical simulations, points represent experimental data.

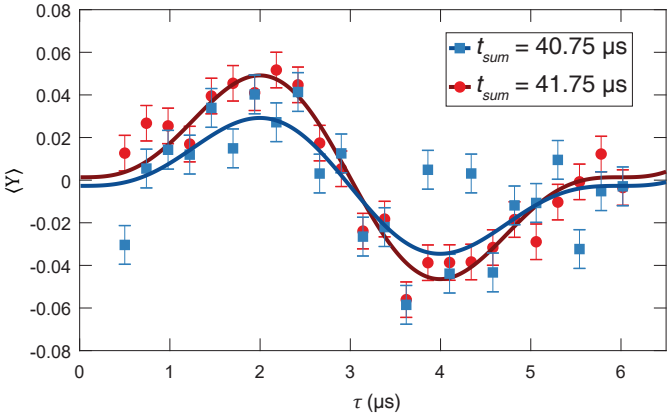

FIG. S15. PSE measurements taken without compensation. Each set is an average over six measurements using the same t_{sum} but different t_{wait}, evenly sampled over the range of 8-11 μs, i.e. a nuclear Larmor period. The curves are best fits to the QPS signal, allowing an offset. Many of the anomalous points in our data taken without compensation are repeatable.

B. Supporting measurements

To motivate the need for compensation in our system, we present measurements analogous to the simulations in Fig. 3 of the main text. Using the same $t_{SL} = 3$ μs, we perform PSE measurements without compensation for $t_{sum} = 40.75$ μs and 41.75 μs, displayed in Fig. S15. Each sequence is repeated for six different values of t_{wait} evenly spaced over a 3-μs range, and all six are aggregated to approximately average over t_{wait}. As nuclear polarization decays negligibly on the scale of t_{sum}, we might naively expect the polarization to be the same for both curves. Instead, the amplitude of the curve for $t_{sum} = 41.75$ μs is roughly 50% larger. We do not expect quantitative agreement with Fig. S12 given the sensitive dependence on t_{sum} (see also Fig. S13), the difficulty in smoothly averaging over t_{wait}, and minor differences in how sequences are practically implemented, but the data do show evidence for global sequence parameters like t_{sum} playing an important role in the nuclear steady state polarization when compensation is neglected. In addition, some anomalous points appear especially in the set for $t_{sum} = 40.75$ μs. Though not predicted in simulation, these anomalous points are often repeatable in our data taken without compensation and complicate the interpretation of those data sets.

VII. THEORETICAL DERIVATIONS OF NV SPIN-ECHO DYNAMICS DUE TO POLARIZED NUCLEAR SPIN BATHS

In Appendix A, we derive the dynamics of a sensor qubit due to a generic bath with interaction-picture qubit-bath coupling operator $\hat{\xi}(t) \equiv e^{i\hat{H}_{\rm b,i}t}\hat{\xi}e^{-i\hat{H}_{\rm b,i}t}$, which can be written formally as

$$\frac{\langle\hat{\sigma}_-(t_f)\rangle}{\langle\hat{\sigma}_-(0^+)\rangle} = \mathrm{Tr}\left\{\hat{U}_{\mathrm{I},\uparrow}(t_f)\,\hat{\rho}_{\rm b,i}\hat{U}^\dagger_{\mathrm{I},\downarrow}(t_f)\right\}, \tag{S7}$$

$$\hat{U}_{\mathrm{I},\uparrow/\downarrow}(t_f) \equiv \mathcal{T}e^{\pm\frac{i}{2}\int_0^{t_f}dt'[F(t)\pm1]\hat{\xi}(t')}. \tag{S8}$$

Our goal is to relate the qubit coherence function $\langle\hat{\sigma}_-(t_f)\rangle$ to the polarizations of the bath. To achieve this, generally one can perform a perturbative expansion of the qubit decoherence factor $\mathcal{K}(t_f)$ in terms of the bath coupling operator, where we define

$$\mathcal{K}(t_f) \equiv \ln\frac{\langle\hat{\sigma}_-(t_f)\rangle}{\langle\hat{\sigma}_-(0^+)\rangle} = -\chi(t_f) - i\Phi(t_f). \tag{S9}$$

Note that if the qubit were coupled to a classical stochastic variable $\xi(t)$, then the corresponding $\mathcal{K}(t_f)$ function would be give by the cumulant generating function (CGF) of $\xi(t)$. For the quantum operator $\hat{\xi}(t)$, $\mathcal{K}(t_f)$ in turn corresponds to the Keldysh-order CGF of the $\hat{\xi}(t)$, so that we can utilize the Keldysh approach to systematically expand the CGF in orders of the bath coupling operator (see e.g. [7] for a pedagogical discussion). Using the Keldysh formalism, the quantum operator $\hat{\xi}(t)$ is captured by a classical $\xi_{\rm cl}(t)$ and quantum field $\xi_{\rm q}(t)$, so that $\mathcal{K}(t_f)$ can be computed as

$$\mathcal{K}(t_f) = \sum_{\ell=1}^{\infty}\sum_{m=0}^{\infty}\frac{(-i)^{\ell+m}}{\ell!m!}\mathcal{K}^{(\ell,m)}(t_f), \tag{S10}$$

$$\mathcal{K}^{(\ell,m)}(t_f) = \frac{1}{2^m}\prod_{j=1}^{\ell}\left[\int_0^{t_f}dt_jF(t_j)\right]\prod_{k=\ell+1}^{\ell+m}\left[\int_0^{t_f}dt_k\right]C^{(\ell,m)}(t_1,\ldots,t_{\ell+m}), \tag{S11}$$

where $C^{(\ell,m)}(t_1,\ldots,t_{\ell+m})$ denote the Keldysh-ordered cumulants, which can be obtained from Keldysh-ordered moments of the form $\overline{\xi_{\rm cl}(t_1)\ldots\xi_{\rm cl}(t_\ell)\xi_{\rm q}(t_{\ell+1})\ldots\xi_{\rm q}(t_{\ell+m})}$ and lower-order averages. If the bath is Gaussian, i.e. the quantum $\xi_{\rm q}(t)$ and classical $\xi_{\rm cl}(t)$ fields when viewed as stochastic variables follow a Gaussian distribution, then the noise and response properties of the bath can be fully captured via the first- and the second-order cumulants, so that we can exactly compute the dynamics of the sensor qubit as

$$\chi_{\rm Gaus}(t_f) = \frac{1}{2}\mathcal{K}^{(2,0)}(t_f) = \frac{1}{2}\int_0^{t_f}dt_1F(t_1)\int_0^{t_f}dt_2F(t_2)\overline{\delta\xi_{\rm cl}(t_1)\delta\xi_{\rm cl}(t_2)}, \tag{S12}$$

$$\Phi_{\rm Gaus}(t_f) = \mathcal{K}^{(1,0)}(t_f) - i\mathcal{K}^{(1,1)}(t_f) = \int_0^{t_f}dt_1F(t_1)\overline{\xi_{\rm cl}(t_1)} - \frac{i}{2}\int_0^{t_f}dt_1F(t_1)\int_0^{t_f}dt_2\overline{\delta\xi_{\rm cl}(t_1)\delta\xi_{\rm q}(t_2)}. \tag{S13}$$

Note that Eqs. (S12) and (S13) reproduce Eqs. (A18-A20) in Appendix A.

As we show, in the regime where the qubit does not have a strongly coupled bath nuclear spin, and in the short-time limit, we can effectively treat the spin bath as Gaussian. Physically, this corresponds to the regime where the bath approximately satisfies the central limit theorem. More specifically, for Gaussian baths, we can compute the qubit phase shift $\Phi(t_f)$ as follows

$$\Phi(t_f) = \Phi_m(t_f) + \Phi_q(t_f), \tag{S14}$$

$$\Phi_m(t_f) = \int_0^{t_f}dt_1F(t_1)\langle\hat{\xi}(t_1)\rangle, \tag{S15}$$

$$\Phi_q(t_f) = -\frac{1}{2}\int_0^{t_f}dt_1F(t_1)\int_0^{t_1}dt_2G^R_{\xi\xi}(t_1,t_2). \tag{S16}$$

Specifically for Nitrogen-Vacancy (NV) center coupled to nuclear spin bath, as we discuss below, one can further use the interplay between two distinct phase shifts in Eq. (S14) to detect both axial and transverse components of bath polarization with respect to the external magnetic field. We also show the response function in this case is directly related to the spin bath polarization.

We start by considering a single NV center coupled to its surrounding ^{13}C nuclear spin bath, with the total system in an external magnetic field along the NV axis. For convenience, we choose the quantization axes of nuclear spins such that the nuclear spin z axis is parallel to the magnetic field. Thus, the bath-only Hamiltonian is given by

$$\hat{H}_{\mathrm{b,i}} = \omega_L \sum_j \hat{I}_{z,j}, \tag{S17}$$

where $\hat{I}_{\alpha,j}$ ($\alpha = x, y, z$) denote the standard spin operators of jth bath spin. We further choose the nuclear spin x axes such that the NV-nuclear interaction can be written as

$$\hat{\xi} = -\sum_j \left(A_{\parallel,j} \hat{I}_{z,j} + A_{\perp,j} \hat{I}_{x,j} \right). \tag{S18}$$

Note that under this convention, the nuclear spin x axes are in general distinct between different bath spins and may not be related to any specific geometrical axis. Let us now discuss the justification of the Gaussian approximation, where we truncate Eq. (S10) at the second order ($\ell + m = 2$, c.f. Eqs. (S12) and (S13)). Noting that the interaction-picture bath coupling operator in this case is given by ($\hat{I}_{+,j} \equiv \hat{I}_{x,j} \pm i\hat{I}_{y,j}$)

$$\hat{\xi}(t) = -\sum_j \left[A_{\parallel,j} \hat{I}_{z,j} + \frac{A_{\perp,j}}{2} (\hat{I}_{+,j} e^{i\omega_L t} + \mathrm{H.c.}) \right], \tag{S19}$$

and plugging Eq. (S19) into Eq. (S10), one can mathematically show that (up to other $o(1)$ factors that depend on initial bath states and trigonometric functions) contributions of higher-order terms in the Keldysh CGF are controlled by a set of dimensionless factors: $\omega_L t_f$, $\frac{A_{\parallel,j}}{\omega_L}$ and $\frac{A_{\parallel,j}}{\omega_L}$. Thus, the qubit dynamics is dominated by the Gaussian contributions if the following conditions are met:

$$\omega_L t_f < 1, \quad \frac{A_{\parallel,j}}{\omega_L} < 1, \quad \frac{A_{\perp,j}}{\omega_L} < 1. \tag{S20}$$

We thus obtain the necessary condition $A_{\parallel,j} t_f \lesssim 1, A_{\perp,j} t_f \lesssim 1$ quoted in the main text for the Gaussian approximation to accurately describe the nuclear spin baths probed in our experiments. As a concrete example, we consider the specific case where the initial bath state is a product state of individual nuclear spins, each with a polarization along the z axis. The initial bath state can now be written as

$$\hat{\rho}_{\mathrm{b,i}} = \bigotimes_\ell \left(\frac{\hat{\sigma}_{\ell,0} + p_{z,\ell} \hat{\sigma}_{\ell,z}}{2} \right), \tag{S21}$$

and the leading order non-Gaussian contribution to the phase shift can be computed explicitly as

$$\Phi^{(3)}(t_f) = \sum_j p_{z,j} \frac{A_{\perp,j}^2}{\omega_L^2} \frac{A_{\parallel,j}}{\omega_L} \left(\frac{\omega_L t_f}{4} \sin^2 \frac{\omega_L t_f}{2} - 2 \sin^2 \frac{\omega_L t_f}{4} \sin \frac{\omega_L t_f}{2} \right). \tag{S22}$$

We note that the relative magnitude of the non-Gaussian phase in Eq. (S22) with respect to the Gaussian contributions (see Eq. (S35)) is indeed controlled by the factors in Eq. (S20); however, the validity of Eq. (S20) is general and extends beyond the specific example here. Eq. (S20) can be intuitively understood as imposing two independent set of conditions:

- there is no strongly coupled bath spin (i.e. there is no individual bath spin whose interaction strength with the qubit is much stronger that the qubit couplings with all the other bath spins);
- the evolution time is sufficiently short.

If either one of these two criteria is not satisfied, then the bath cannot be assumed to satisfy the central limit theorem. It is also worth noting that the inequalities in Eq. (S20) involve individual coupling strengths between each bath spin and the qubit (instead of their sum); this also agrees with the physical intuition that if the qubit is simultaneously coupled to multiple spins with similar interaction strengths, then the bath approaches the Gaussian regime in the limit of large spin bath size.

We now show the short-time qubit coherence function under Hahn echo or more general dynamical decoupling sequences allows extraction of bath properties. In this case, we can safely ignore any intrabath interactions. We also focus on the regime where the nuclear spin environment can be well approximated as Gaussian; otherwise, the NV

dynamics would be dominated by effects due to one or few closest spins, in which case the nuclear spins should be treated as coherent spin registers rather than a noisy environment. Without loss of generality, we can restrict to NV spin subspace with $\{m_s = 0, m_s = -1\}$ and map it to a probe qubit with $|m_s = 0\rangle \Rightarrow |\downarrow\rangle$ and $|m_s = -1\rangle \Rightarrow |\uparrow\rangle$, so that the NV-bath Hamiltonian can be written as

$$\hat{H}_{\rm tot} = |\downarrow\rangle\langle\downarrow| \otimes \hat{H}_{\rm b,i} + |\uparrow\rangle\langle\uparrow| \otimes (\hat{H}_{\rm b,i} + \hat{\xi}). \tag{S23}$$

As the dynamical nuclear polarization protocols can in general generate bath polarizations along both the parallel (z) and transverse (x, y) directions, we assume that at the beginning of the Hahn echo protocol, the initial bath state is given by a generic product state as

$$\hat{\rho}_{\rm b,i} = \bigotimes_j \hat{\rho}_{{\rm i},j}, \quad \hat{\rho}_{{\rm i},j} = \frac{1}{2}\left(\hat{\mathbb{I}}_j + \sum_{\alpha=x,y,z} p_{\alpha,j}\hat{\sigma}_{\alpha,j}\right). \tag{S24}$$

However, the results obtained in this section also directly generalizes to entangled initial bath states (as long as nuclear-nuclear interactions are negligible). Note that we use the extra nuclear spin index in operators $\hat{\sigma}_{\alpha,j}$ to distinguish them from NV spin operators. We also define the initial nuclear spin bath polarization as

$$p_{\alpha,j} = \langle\hat{\sigma}_{\alpha,j}\rangle, \quad (\alpha = x, y, z). \tag{S25}$$

As such, the qubit coherence function in Eq. (S7) factorizes into contributions from each individual bath spins.

While our approach is generally applicable to more general pulses, for concreteness we focus on the case with Hahn echo, where the switching function is given by

$$F(t) = \begin{cases} +1, & 0 < t \le \frac{t_f}{2}, \\ -1, & \frac{t_f}{2} < t \le t_f. \end{cases} \tag{S26}$$

We now consider the qubit coherence function under Gaussian approximation. The linear order phase shift $\Phi_m(t_f)$ can be directly computed using Eq. (S15), so that we have

$$\Phi_m(t_f) = -\frac{2}{\omega_L}\sin^2\frac{\omega_L t_f}{4}\sum_j A_{\perp,j}p_{\perp,j}\left(\frac{\omega_L t_f}{2}\right), \tag{S27}$$

where for convenience, we define the jth spin polarization projection along direction rotated from y-axis by angle φ in the xy-plane as

$$p_{\perp,j}(\varphi) \equiv p_{x,j}\sin\varphi + p_{y,j}\cos\varphi. \tag{S28}$$

For the second-order contributions, in the Gaussian regime we can compute the dephasing factor $\chi(t_f)$ in Appendix A, or equivalently,

$$\chi(t_f) = \int_0^{t_f} dt_1 F(t_1)\int_0^{t_1} dt_2 F(t_2)\bar{S}(t_1, t_2), \tag{S29}$$

so that we obtain

$$\chi(t_f) = \frac{1}{2}\int_0^{t_f} dt_1 F(t_1)\int_0^{t_1} dt_2 F(t_2)\langle\{\delta\hat{\xi}(t_1), \delta\hat{\xi}(t_2)\}\rangle \tag{S30}$$

$$= 2\frac{\sum_j A_{\perp,j}^2}{\omega_L^2}\sin^4\frac{\omega_L t_f}{4} - \frac{1}{2}\left[\Phi_m(t_f)\right]^2. \tag{S31}$$

The quench phase shift $\Phi_q(t_f)$ can be similarly calculated using Eq. (S16)

$$\Phi_q(t_f) = \sum_j p_{z,j}\frac{A_{\perp,j}^2}{\omega_L^2}\sin^2\frac{\omega_L t_f}{4}\sin\frac{\omega_L t_f}{2} + \frac{2}{\omega_L^2}\sin^2\frac{\omega_L t_f}{4}\sum_j A_{\perp,j}A_{\parallel,j}\,p_{\perp,j}\left(\frac{\omega_L t_f}{2}\right)$$
$$- \sin\frac{\omega_L t_f}{4}\sum_j \frac{A_{\perp,j}}{\omega_L}\frac{A_{\parallel,j}t_f}{2}\,p_{\perp,j}\left(\frac{3\omega_L t_f}{4}\right). \tag{S32}$$

In the experiments, we mainly focus on the short-time regime so that $|A_{\parallel,j}|t_f \ll 1$. For the dynamical nuclear polarization protocol used in the experiments, it is also a good approximation to assume that the parallel component dominates over transverse polarization, so that we can further simplify Eq. (S31) as

$$\chi(t_f) \simeq 2\sum_j \frac{A_{\perp,j}^2}{\omega_L^2}\sin^4\frac{\omega_L t_f}{4}. \tag{S33}$$

Thus, measuring the short-time qubit dephasing behavior for spin bath with weak or zero polarization lets us extract the effective qubit-bath transverse coupling coefficient

$$\epsilon \equiv \sum_j \frac{A_{\perp,j}^2}{\omega_L^2}. \tag{S34}$$

For the phase shift dynamics, at first glance it may seem difficult to separate the contributions from the axial and transverse polarization within the total phase shift, which can now be written as

$$\begin{aligned}\Phi_{\rm Gaus}(t_f) =&\Phi_m(t_f)+\Phi_q(t_f)\\ =&\sum_j p_{z,j}\frac{A_{\perp,j}^2}{\omega_L^2}\sin^2\frac{\omega_L t_f}{4}\sin\frac{\omega_L t_f}{2}-\frac{2}{\omega_L^2}\sin^2\frac{\omega_L t_f}{4}\sum_j A_{\perp,j}(\omega_L-A_{\parallel,j})p_{\perp,j}\left(\frac{\omega_L t_f}{2}\right)\\ &-\sin\frac{\omega_L t_f}{4}\sum_j\frac{A_{\perp,j}}{\omega_L}\frac{A_{\parallel,j}t_f}{2}p_{\perp,j}\left(\frac{3\omega_L t_f}{4}\right).\end{aligned} \tag{S35}$$

Specifically, even if the parallel components dominate, i.e. we can assume $|p_{z,j}| \gg \sqrt{p_{x,j}^2+p_{y,j}^2}$, the linear-order term $\Phi_m(t_f)$ that solely depends on the transverse polarization can still be comparable to the quench phase shift $\Phi_q(t_f)$, making it challenging to distinguish between two effects. Fortunately, for the NV system we can design the sensing sequence to rotate the transverse polarization through varying angles in the equatorial (x,y) plane, in which case the net phase is given by

$$\begin{aligned}\Phi_{\rm Gaus}(t_f;\theta) =&\sum_j p_{z,j}\frac{A_{\perp,j}^2}{\omega_L^2}\sin^2\frac{\omega_L t_f}{4}\sin\frac{\omega_L t_f}{2}-\frac{2}{\omega_L^2}\sin^2\frac{\omega_L t_f}{4}\sum_j A_{\perp,j}(\omega_L-A_{\parallel,j})p_{\perp,j}\left(\frac{\omega_L t_f}{2}+\theta\right)\\ &-\sin\frac{\omega_L t_f}{4}\sum_j\frac{A_{\perp,j}}{\omega_L}\frac{A_{\parallel,j}t_f}{2}p_{\perp,j}\left(\frac{3\omega_L t_f}{4}+\theta\right).\end{aligned} \tag{S36}$$

As such, averaging over the total phase $\Phi_{\rm Gaus}(t_f;\theta)$ sampled over the entire xy-plane lets us cancel out the contributions from transverse polarization, and through that process extract the quench phase shift contribution due to z polarization:

$$\Phi_q(t_f)\big|_{p_{x,j}=p_{y,j}=0} = \int_0^{2\pi}\Phi_{\rm Gaus}(t_f;\theta)d\theta \tag{S37}$$

$$\begin{aligned}=&\sum_j p_{z,j}\frac{A_{\perp,j}^2}{\omega_L^2}\sin^2\frac{\omega_L t_f}{4}\sin\frac{\omega_L t_f}{2}\\ \equiv&\epsilon\overline{p}_z\sin^2\frac{\omega_L t_f}{4}\sin\frac{\omega_L t_f}{2}.\end{aligned} \tag{S38}$$

Combining Eq. (S38) with Eq. (S33), we obtain a model-independent measure of axial (z) polarization, weighted by the coupling coefficients $A_{\perp,j}$, as

$$\overline{p}_z = \frac{\sum_j p_{z,j}A_{\perp,j}^2}{\sum_j A_{\perp,j}^2}. \tag{S39}$$

Furthermore, the oscillation amplitude of $\Phi_{\rm Gaus}(t_f;\theta)$ versus angle θ also lets us extract a rough estimate for the average of transverse polarizations weighted over qubit-bath couplings.

[1] P. L. Stanwix, L. M. Pham, J. R. Maze, D. Le Sage, T. K. Yeung, P. Cappellaro, P. R. Hemmer, A. Yacoby, M. D. Lukin, and R. L. Walsworth, *Coherence of nitrogen-vacancy electronic spin ensembles in diamond*, Phys. Rev. B **82**, 201201 (2010).

[2] M. Onizhuk and G. Galli, *PyCCE: A Python Package for Cluster Correlation Expansion Simulations of Spin Qubit Dynamics*, Adv. Theory Simul. **4**, 2100254 (2021).
[3] T. H. Taminiau, J. J. T. Wagenaar, T. van der Sar, F. Jelezko, V. V. Dobrovitski, and R. Hanson, *Detection and Control of Individual Nuclear Spins Using a Weakly Coupled Electron Spin*, Phys. Rev. Lett. **109**, 137602 (2012).
[4] J. Scheuer, I. Schwartz, S. Müller, Q. Chen, I. Dhand, M. B. Plenio, B. Naydenov, and F. Jelezko, *Robust techniques for polarization and detection of nuclear spin ensembles*, Phys. Rev. B **96**, 174436 (2017).
[5] P. C. Maurer, G. Kucsko, C. Latta, L. Jiang, N. Y. Yao, S. D. Bennett, F. Pastawski, D. Hunger, N. Chisholm, M. Markham, *et al.*, *Room-temperature quantum bit memory exceeding one second*, Science **336**, 1283 (2012).
[6] K. Ohno, F. J. Heremans, L. C. Bassett, B. A. Myers, D. M. Toyli, A. C. Bleszynski Jayich, C. J. Palmstrøm, and D. D. Awschalom, *Engineering shallow spins in diamond with nitrogen delta-doping*, Appl. Phys. Lett. **101**, 082413 (2012).
[7] Y.-X. Wang and A. A. Clerk, *Spectral characterization of non-Gaussian quantum noise: Keldysh approach and application to photon shot noise*, Phys. Rev. Res. **2**, 033196 (2020).